Naval Research Laboratory
Washington, DC 20375-5320

U.S. NAVAL RESEARCH LABORATORY

NRL/6041/MR—2022/3

Coupled CFD and Structural Solver for Flapping Wing Simulations

RAVI RAMAMURTI

JASON GEDER

KAMAL VISWANATH

Laboratory for Propulsion, Energetic, and Dynamic Systems Branch
Laboratory for Computational Physics and Fluid Dynamics Division

PROF. RAINALD LÖHNER

CFD Center
George Mason University
Fairfax, VA

ORLANDO SOTO

Applied Simulations, Inc.
McLean, VA

October 12, 2022

REPORT DOCUMENTATION PAGE

Form Approved
OMB No. 0704-0188

1. REPORT DATE *(DD-MM-YYYY)*	**2. REPORT TYPE**	**3. DATES COVERED** *(From - To)*
12-10-2022	NRL Memorandum Report	October 2019 – September 2021

4. TITLE AND SUBTITLE

Coupled CFD and Structural Solver for Flapping Wing Simulations

5a. CONTRACT NUMBER

5b. GRANT NUMBER

5c. PROGRAM ELEMENT NUMBER

6. AUTHOR(S)

Ravi Ramamurti, Jason Geder, Kamal Viswanath, Prof. Rainald Löhner*, and Orlando Soto**

5d. PROJECT NUMBER

5e. TASK NUMBER

5f. WORK UNIT NUMBER
1J26

7. PERFORMING ORGANIZATION NAME(S) AND ADDRESS(ES)

Naval Research Laboratory
4555 Overlook Avenue, SW
Washington, DC 20375-5320

8. PERFORMING ORGANIZATION REPORT NUMBER

NRL/6041/MR--2022/3

9. SPONSORING / MONITORING AGENCY NAME(S) AND ADDRESS(ES)

Naval Research Laboratory
4555 Overlook Avenue, SW
Washington, DC 20375-5320

10. SPONSOR / MONITOR'S ACRONYM(S)

NRL 6.1 Base Program

11. SPONSOR / MONITOR'S REPORT NUMBER(S)

12. DISTRIBUTION / AVAILABILITY STATEMENT

DISTRIBUTION STATEMENT A: Approved for public release; distribution is unlimited.

13. SUPPLEMENTARY NOTES

*CFD Center, George Mason University 4400 University Dr, Fairfax, VA 22030
**Applied Simulations, Inc. 1211 Pine Hill Rd, McLean, VA 22101

14. ABSTRACT

A fluid structure interaction modeling tool is developed for the simulation of thrust generation using flexible flapping wings. Three models are developed by coupling the computational fluid dynamics (CFD) solver with different computational structural dynamics (CSD) solvers. The first model, a coupled solver based on eigenmodes is validated using the well-known Turek-Hron benchmark problem. The second model, a coupled solver for membrane cases is developed and tested for 2-D flow cases at various angles of attack and compared with results in the literature. The third model, a comprehensive structural solver coupled to the CFD solver is developed and tested for a flapping wing comprised of carbon fiber spars with mylar membrane between them. Several parametric studies are performed for this configuration varying the stroke amplitude and flapping frequency of the wing.

15. SUBJECT TERMS

Fluid dynamics Structural analysis Fluid-structure interaction
Multiphysics Flapping wings.

16. SECURITY CLASSIFICATION OF:			**17. LIMITATION OF ABSTRACT**	**18. NUMBER OF PAGES**	**19a. NAME OF RESPONSIBLE PERSON**
					Ravi Ramamurti
a. REPORT	**b. ABSTRACT**	**c. THIS PAGE**	U	21	**19b. TELEPHONE NUMBER** *(include area code)*
U	U	U			(202) 767-0608

This page intentionally left blank.

Table of Contents

List of Figures

Coupled CFD and Structural solver for Simulation of Flapping Wing Analysis

INTRODUCTION

Unmanned air vehicles (UAVs) and unmanned underwater vehicles (UUVs) are becoming ubiquitous, and the technologies that drive their development are pushing the envelope of viable mission profiles for these systems. Finding solutions to achieve effective and efficient flight performance in unpredictable flow regimes such as urban areas and cluttered indoor environments is essential to future UAVs, and also to UUVs in littoral regions and close to marine infrastructures. As the demand for these small vehicles grow due to the missions they enable, there is a need to rethink the design to achieve the desired performance. In nature, larger flying animals tend to rely on their wings to glide or soar, and these wings provided some of the inspiration for early aircraft design. However, smaller flying animals rely more heavily on wing flapping to create the lift and control forces needed for flight, and this is an area that holds promise for small UAVs and UUVs.

Smaller flying animals such as hummingbirds and bees rely mainly on wing flapping for lift generation, as opposed to gliding. Scientists and engineers have employed a mix of biological, prototype and computational studies to understand the wing mechanisms and kinematics of species ranging from fruit flies to hummingbirds to bats. The accumulation of these efforts has led to an understanding of the flow physics for different wing geometries, configurations, and kinematics for both hover and forward flight, as described by Ramamurti and Sandberg [1,2] and Viswanath et al. [3]. The decreasing size of the UAVs and UUVs makes them susceptible to the fluctuating magnitude and direction of gusts or vortices. Flapping wings hold promise for controlling transient dynamics of smaller vehicles in complex environments. Improved modeling of wing surface stretching and other deformations is needed to determine the extent to which flexible wing surfaces contribute to the agility of flying animals and to provide guidance in materials selection and wing shape and kinematics design for flying vehicles.

We have previously conducted computational studies of flapping wings and flapping wing platforms, and compared results of these studies with experimental data from both biological and man-made wing counterparts, see Ramamurti et al. [4,5]. However, while these comparisons proved useful for aiding the process of designing bio-inspired UAV and UUV platforms, the accuracy of the simulated wing kinematics suffered from a lack of a proper wing deformation models. This weakness pointed to the need to develop a fluid-structure interaction (FSI) capability. In this report, we discuss the development and validation of a fluid-structure interaction solver. This solver is validated against two benchmark test cases.

THE INCOMPRESSIBLE FLOW SOLVER

The governing equations employed are the incompressible Navier-Stokes equations in Arbitrary Lagrangian-Eulerian (ALE) formulation which are written as,

$$\rho \mathbf{v}_{,t} + \rho \mathbf{v}_a \nabla \mathbf{v} + \boldsymbol{\nabla} p = \nabla \mu \nabla \mathbf{v} \quad , \tag{1}$$

$$\nabla . \mathbf{v} = 0 \quad , \tag{2}$$

where p denotes the pressure, $\mathbf{v}_a = \mathbf{v} - \mathbf{w}$ is the advective velocity vector, where $\mathbf{v}$ is the flow velocity and $\mathbf{w}$ is the mesh velocity and μ is the turbulent viscosity. Thus, the equations are Eulerian for zero mesh velocity and Lagrangian if the mesh velocity is the same as the flow velocity. The present time-accurate flow solver uses a spatial discretization based on a Galerkin

Manuscript approved September 30, 2022.

procedure with linear tetrahedral elements, and a temporal discretization based on fractional steps for velocities and pressure. The details of the flow solver have already been discussed extensively elsewhere (Ramamurti et. al. [6-7]) in connection with successfully validated solutions for numerous 2-D and 3-D, laminar and turbulent, steady and unsteady flow problems.

Coupling Structural Solver to CFD

The coupling of the fluid flow and the elastic structural deformation can be carried out in two ways. The first method discretizes the structure using finite elements but assumes that only small elastic deformations occur. Based on the finite element model, a modal decomposition is carried out, and the eigenmodes of the structure are obtained. These eigenmodes are then coupled to the fluid solver. The second strategy involves discretizing the structure using finite elements and solving the structural deformation in a time-accurate manner based on the physical properties. Note that while in the first method only principal eigenmodes are used, in the second method all the eigenmodes that can be seen by the discretization are present, i.e., the maximum possible amount of information is used.

The discretization of the elastic structure via finite elements results in the system,

$$\mathbf{M}\ddot{\mathbf{w}} + \mathbf{D}\dot{\mathbf{w}} + \mathbf{K}\mathbf{w} = \mathbf{f} \quad , \tag{3}$$

where **M**, **D**, and **K** are the mass, damping and stiffness matrices, respectively, **w** is the vector of nodal displacement and **f** is the external force. The matrices **M** and **K** are symmetric positive definite, and can be used to obtain a system of eigenmodes by solving the eigenvalue problem,

$$(-\omega_i^2\mathbf{M} + \mathbf{K}) \cdot e^i = 0, \;\; i = 1, n \quad . \tag{4}$$

The vector of unknowns **w** can be written in terms of the eigenvectors as

$$\mathbf{w} = e^i a_i, \tag{5}$$

resulting in

$$\mathbf{M}e^i\ddot{a}_i + \mathbf{D}e^i\dot{a}_i + \mathbf{K}e^i a_i = \mathbf{f} \quad . \tag{6}$$

Assuming $e^j\mathbf{D}e^i = d^{ii}\delta^{ij}$, we can decompose Eq. (5) by multiplying with e^j, and using the orthogonality properties of **M** and **K**,

$$e^j\mathbf{M}e^i = \delta^{ij}, \text{ and } e^j\mathbf{K}e^i = \omega_i^2\delta^{ij} \quad , \tag{7}$$

where δ^{ij} is the Kronecker delta. This results in a decoupled system of ordinary differential equations

$$\ddot{a}_j + d^{jj}\dot{a}_j + \omega_j^2 a_j = f^j = \mathbf{f} \cdot e^j \quad . \tag{8}$$

This system of ODEs can be solved either given the forcing loads **f** resulting in the nodal displacement **w**, or given the motion a_i, resulting in the nodal displacement **w**. In some cases, the eigenvectors are not scaled according to Eq. (7). Instead, they are of the form

$$\boldsymbol{j}^i = \alpha^i e^i \quad , \tag{9}$$

and the nodal displacement **w** is written as

$$\mathbf{w} = \boldsymbol{j}^i b_i, \tag{10}$$

resulting in

$$\ddot{b}_i + d^{ii}\dot{b}_i + \omega_i^2 b_i = \frac{1}{(\alpha^i)^2}\mathbf{f} \cdot \boldsymbol{j}^i \quad . \tag{11}$$

The scaling factor α^i can be obtained by applying a known force and matching the corresponding displacements and is used as an input in coupling the modes with the CFD solver. If we consider beam elements, the basic equation is

$$\rho A\ddot{w} + EI\, w_{,xxxx} = q \ , \tag{12}$$

where w is the displacement, ρ is the density, A is the cross-sectional area of the beam, E is the Young's modulus, I is the area moment of the beam and q is the force per unit length. The eigenfunctions for this system can be written as

$$w = w_0 w_s(\lambda x), \ \ w_{,xxxx} = \lambda^4 w \ . \tag{13}$$

Substituting this in Eq. (12) and applying a Galerkin approximation, we get

$$\rho A c_w \ddot{w}_0 + EI\lambda^4 c_w w_0 = \int q w_s(\lambda x)\, dx \,, \quad c_w = \int w_s^2(\lambda dx) dx \ . \tag{14}$$

The force integral can be approximated by point collocation as

$$\int q w_s(\lambda x)\, dx = \sum_i w_s(\lambda x_i)\, F(x_i) \ , \tag{15}$$

resulting in the following eigenmode system

$$m\ddot{w} + kw = \sum_i w_s(\lambda x_i)\, F(x_i) \ , \tag{16}$$

where $m = \rho A c_w$, and $k = EI\lambda^4 c_w$. For different boundary conditions, such as cantilevered beam and free beams, the eigenvalues can be found from standard test books. These are used to validate the coupled solver.

VALIDATION OF THE COUPLED MODEL

Most natural flyers such as bats use an articulated skeleton covered with an elastic membrane for morphing their wings during flight. In this research effort, we consider bio-inspired wings comprised of carbon fiber structures and an elastic Mylar membrane between them. In order to validate the coupled solver, the problem is broken into two parts: one for the coupled fluid and beam case and the second for the coupled fluid and membrane case.

Coupled solver for Beams:

In order to validate the coupled solver for the beam structures, we selected the case described by Turek and Hron [8] of flow around a cylinder with an elastic beam behind the cylinder. The flow is incompressible and in the laminar regime, ranging from Reynolds number, Re = 20 to 200. The overall set up consists of a solid cylinder with the elastic beam submerged in the channel flow. Then self-induced oscillations in the fluid and the beam are monitored and the time-dependent displacements are compared. The coupled solver described above using eigen modes is employed for the simulation. This coupled code was scaled for a cantilevered beam with a point load at the end of the beam. Next, the solver was used to simulate the benchmark case shown in Figure 1. The domain has length L = 2.5m and height H = 0.41m. The center of the cylinder is positioned at (0.2m, 0.2m) measured from the bottom left corner of the channel and the radius of the cylinder is r = 0.05m. The elastic beam has length l =0.35m and height h = 0.02m. The right bottom corner is positioned at (0.6m, 0.19m) and the left end is fully attached to the cylinder. The control point A is attached to the structure and is moving in time with A(0) = (0.6m, 0.2m). Two sets of physical parameters are considered and are shown in Table 1. Here, the $\rho^s, \nu^s,$ and μ^s are the density, Poisson's ratio and dynamic viscosity of the solid, ρ^f and ν^f are the density and kinematic viscosity of the fluid, and $\overline{U}$ is the mean inflow velocity. Defining Reynolds number by $Re = 2r\overline{U}/\nu^f$, the two cases correspond to Re = 20 and 200.

A parabolic inflow velocity profile is prescribed as

$$v_x(0,y) = 1.5\bar{U}\frac{y(H-y)}{(H/2)^2} \quad . \tag{17}$$

	Re = 20	Re = 200
ρ^s [10^3 Kg/m^3]	1	1
ν^s	0.4	0.4
μ^s [10^6 kg/ms^2]	0.5	2.0
ρ^f [10^3 Kg/m^3]	1	1
ν^f [10^{-3} m^2/s]	1	1
$\bar{U}$ [m/s]	0.2	2.0

Table 1. Physical parameters for Coupled CFD and structural solver validation.

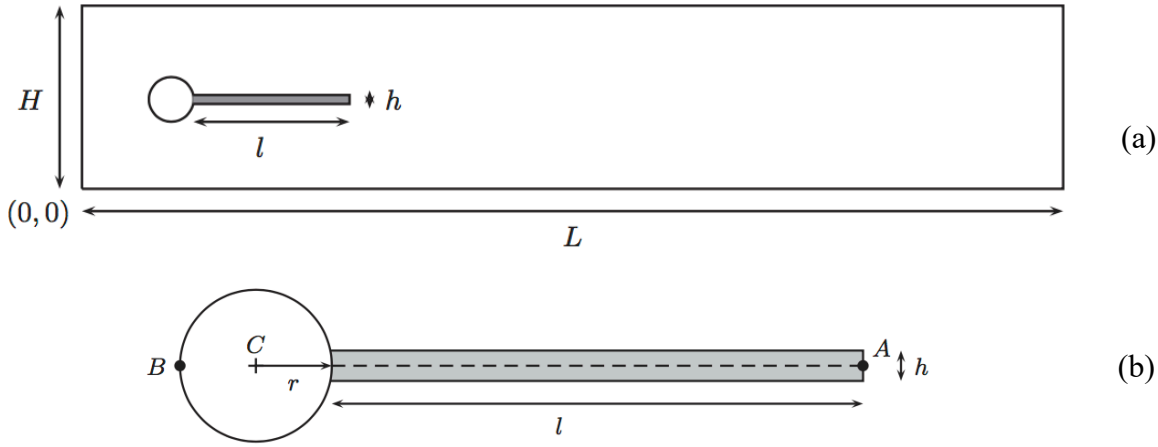

Fig. 1. Turek-Hron benchmark configuration, (a) computational domain and (b) structural details.

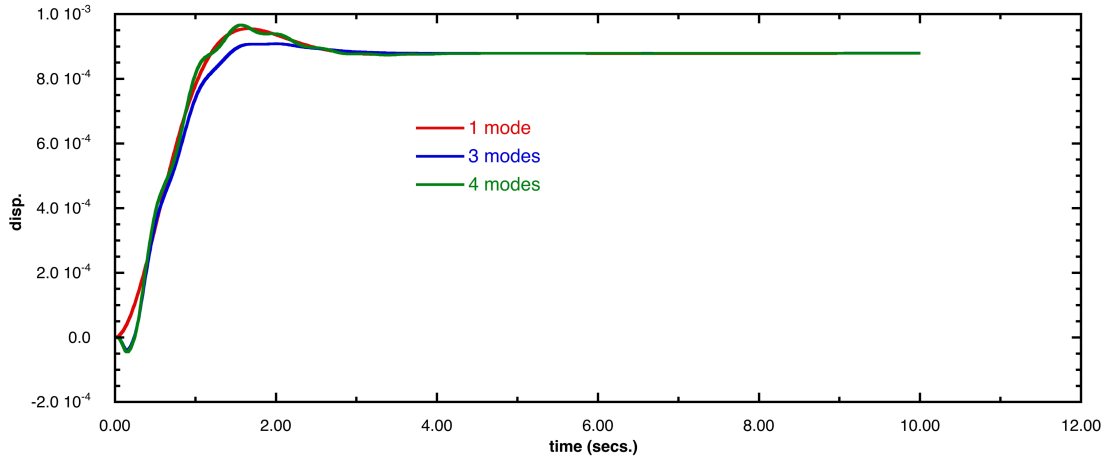

Fig. 2. Displacement time history for the Turek-Hron benchmark case, Re = 20.

Several eigenmodes were included in the coupled solver and for the first test case of Re = 20 all of the modes reached a steady state solution as shown in Fig. 2. The converged displacement is 8.787×10^{-4}m compared to the values of 8.209×10^{-4} reported in [8]. The computed drag and lift, are D =14.25 and L = 0.69, are compared with Turek-Hron's results of D = 14.295 and L =0.76. For the unsteady case of Re = 200, the displacement time history is shown in Fig. 3. The mean displacement is 1.572×10^{-3}m with the range of $\pm 34.21 \times 10^{-3}$m. This is in good agreement with results reported for various coupled solvers reported by Turek et al. [9], which are in the range of $(1.45 - 1.55) \times 10^{-3}$, $\pm 35 \times 10^{-3}$. Figure 4 shows the instantaneous pressure and velocity distribution for the case of Re = 200.

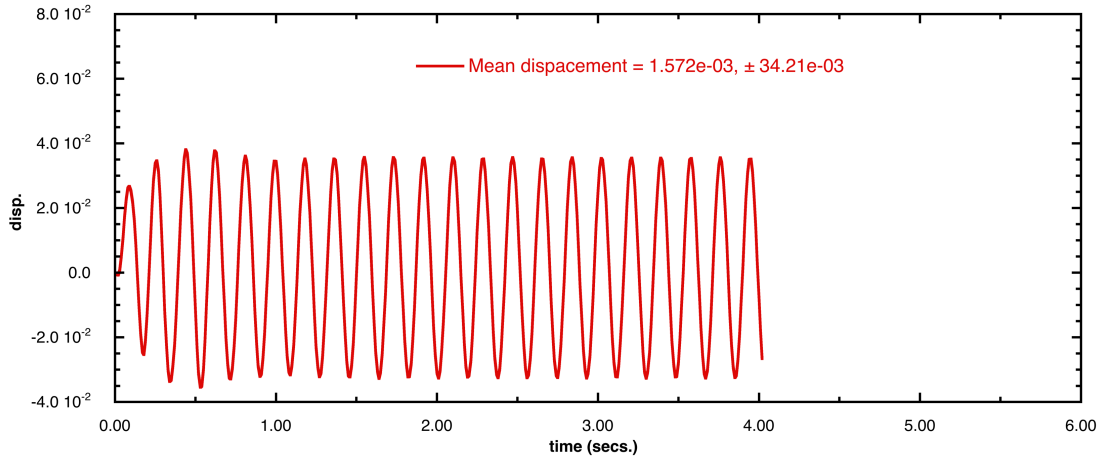

Fig. 3. Displacement time history for the Turek-Hron benchmark case, Re = 200.

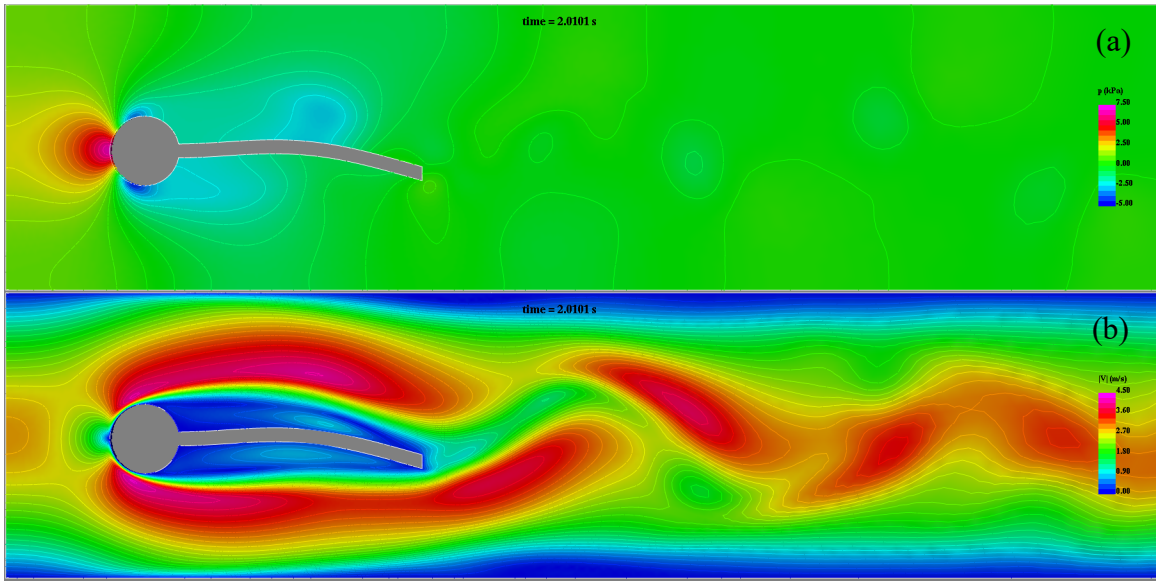

Fig. 4. Flow results for Turek-Hron benchmark case, Re = 200, (a) pressure distribution and (b) magnitude of velocity.

Coupled solver for membranes:

In this case, the structural model employed is based on Smith and Shyy [10] for elastic membranes subjected to a normal force. The governing equation for this model is

$$\rho_s h\ddot{y} + \rho_s c_d \dot{y} + Eh(\delta_0 + \delta)\left[1 + \left(\frac{\partial y}{\partial x}\right)^2\right]^{-\frac{3}{2}} y_{,xx} = \Delta p \quad , \tag{18}$$

where

$$\delta = L - L_0, \quad L = \int_0^{L_0} \sqrt{1 + \left(\frac{\partial y}{\partial x}\right)^2}\, dx \quad . \tag{19}$$

Here, y is the vertical displacement, ρ_s is the density of the membrane, h is the thickeness, c_d is the damping or drag coefficient, E is the modulus of elasticity, L is the length of the membrane, and $\delta$is the increase in length of the membrane. Following the finite element discretization, Eq.18 can be written as

$$\mathbf{M}\ddot{\mathbf{y}} + \mathbf{D}\dot{\mathbf{y}} + \mathbf{K}\mathbf{y} = \mathbf{f} \quad . \tag{20}$$

This system is integrated in time using the implicit Newmark scheme [11] with the parameters β=0.25 and γ=0.5, which is unconditionally stable. The next step is to obtain the integration constants, $b_1$through b_6 as

$$b_1 = \frac{1}{\beta \Delta t^2}\,, b_2 = \frac{1}{\beta \Delta t}\,, b_3 = \frac{1}{2\beta} - 1\,, b_4 = \gamma \Delta t b_1\,,$$
$$b_5 = 1 - \gamma \Delta t b_2\,, b_6 = \Delta t(1 - \gamma b_3 - \gamma) \quad . \tag{21 a-f}$$

Next, the effective stiffness matrix is obtained as

$$\tilde{\mathbf{K}} = \mathbf{K} + b_1\mathbf{M} + b_4\mathbf{D} \quad , \tag{22}$$

And the effective force vector is

$$\tilde{\mathbf{f}} = \mathbf{f} + \mathbf{M}(b_1 y^{n-1} + b_2 \dot{y}^{n-1} + b_3 \ddot{y}^{n-1}) + \mathbf{D}(b_4 y^{n-1} - b_5 \dot{y}^{n-1} - b_3 \ddot{y}^{n-1}) \quad . \tag{23}$$

Next, the new displacements are computed solving

$$\tilde{\mathbf{K}}\, y^{\boldsymbol{n}} = \tilde{\mathbf{f}} \quad , \tag{24}$$

and the new velocities and accelerations are computed using

$$\dot{y}^n = b_4(y^n - y^{n-1}) + b_5\, \dot{y}^{n-1} + b_6\, \ddot{y}^{n-1}$$
$$\ddot{y}^n = b_1(y^n - y^{n-1}) - b_2\, \dot{y}^{n-1} - b_3\, \ddot{y}^{n-1} \quad . \tag{25 a,b}$$

For the validation case for a membrane model of Rojratsirkul et al. [12] was simulated. The membrane airfoil geometry consists of thin latex sheet stretched between a leading edge and a trailing edge mount, shown in Fig. 5. Experimental observations show that the membrane deformation is nearly two-dimensional for the range of angles of attack tested. Simulations were performed for α = 4° to 20°, for structural parameters of Eh = 50, $\rho_s h$ = 0.589, and Re = 2500, as described in Gordnier [13].

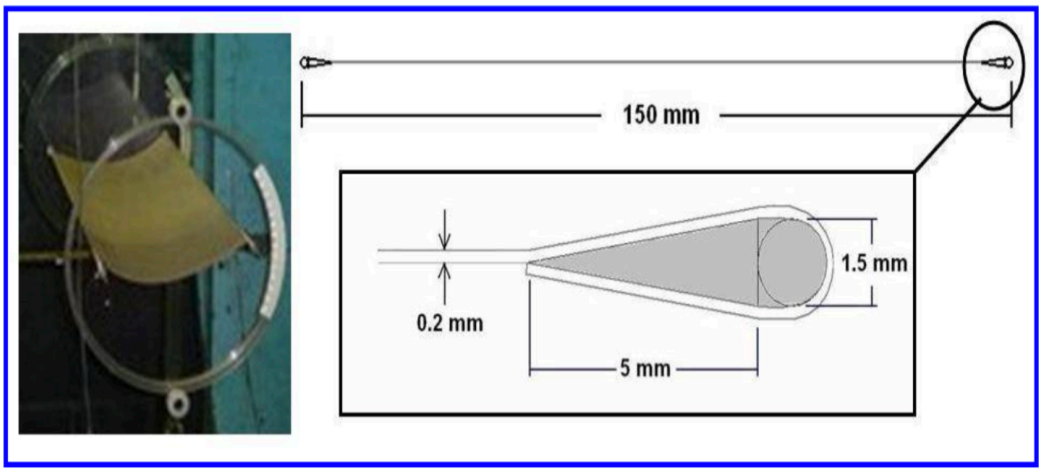

Fig. 5. Membrane Wing Geometry of Rojratsirikul, Wang and Gursul [12].

The mean deflection of the membrane is compared to the computed results of Gordiner [13]. For an angle of attack $\alpha = 4°$, a steady state of the deflection was achieved, and Fig. 6 shows the comparison of the present results. Observe the improvement in the results when the CFD grid is refined form 52.4K points to 124.8K points. For $\alpha = 12°$, both explicit and implicit CFD timestepping schemes were employed for the simulation. Fig. 7a shows the time history of the displacement of the mid-chord, and it is clear that the implicit scheme is unable to capture the unsteady physics. In terms of computational effort, the explicit scheme takes 5 hours on 1 node of an Intel Xeon cluster architecture, compared to 40 minutes for the implicit scheme. Figure 7b shows the comparison of the mean deflection, and the explicit scheme compares well with the results of Gordnier [13]. Figures 8 and 9 show the instantaneous pressure and velocity contours for the implicit and explicit schemes, respectively, and it is clear that the implicit scheme does not capture the unsteady flow field for this higher angle of attack. At $\alpha = 16°$, both explicit and implicit schemes result in a limit cycle oscillation of the mid chord point, with the higher mean and amplitude from the explicit scheme, as shown in Fig. 10a. Fig 10b shows the comparison is better for the implicit scheme. For $\alpha = 20°$, the explicit scheme does not converge into a limit cycle

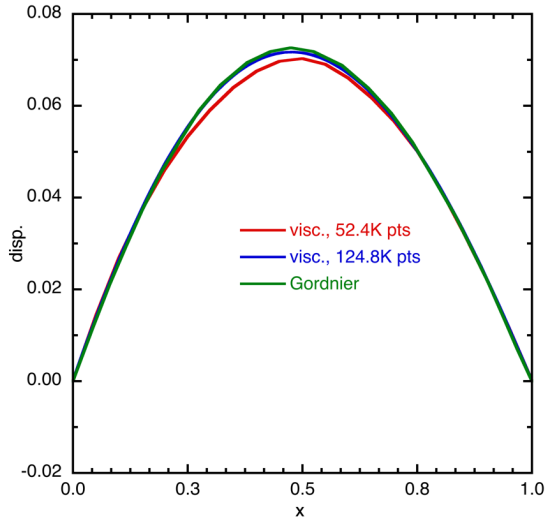

Fig. 6. Mean deflection of the membrane at $\alpha = 4°$.

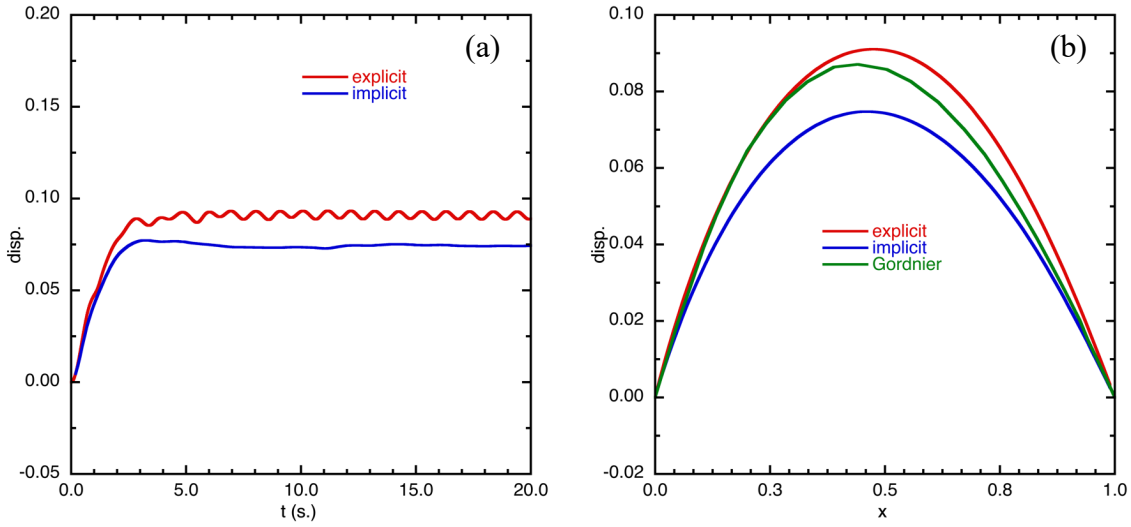

Fig. 7. Results for the membrane deflection for α = 12°, (a) comparison of the mid-chord displacement, and (b) comparison of the mean deflection.

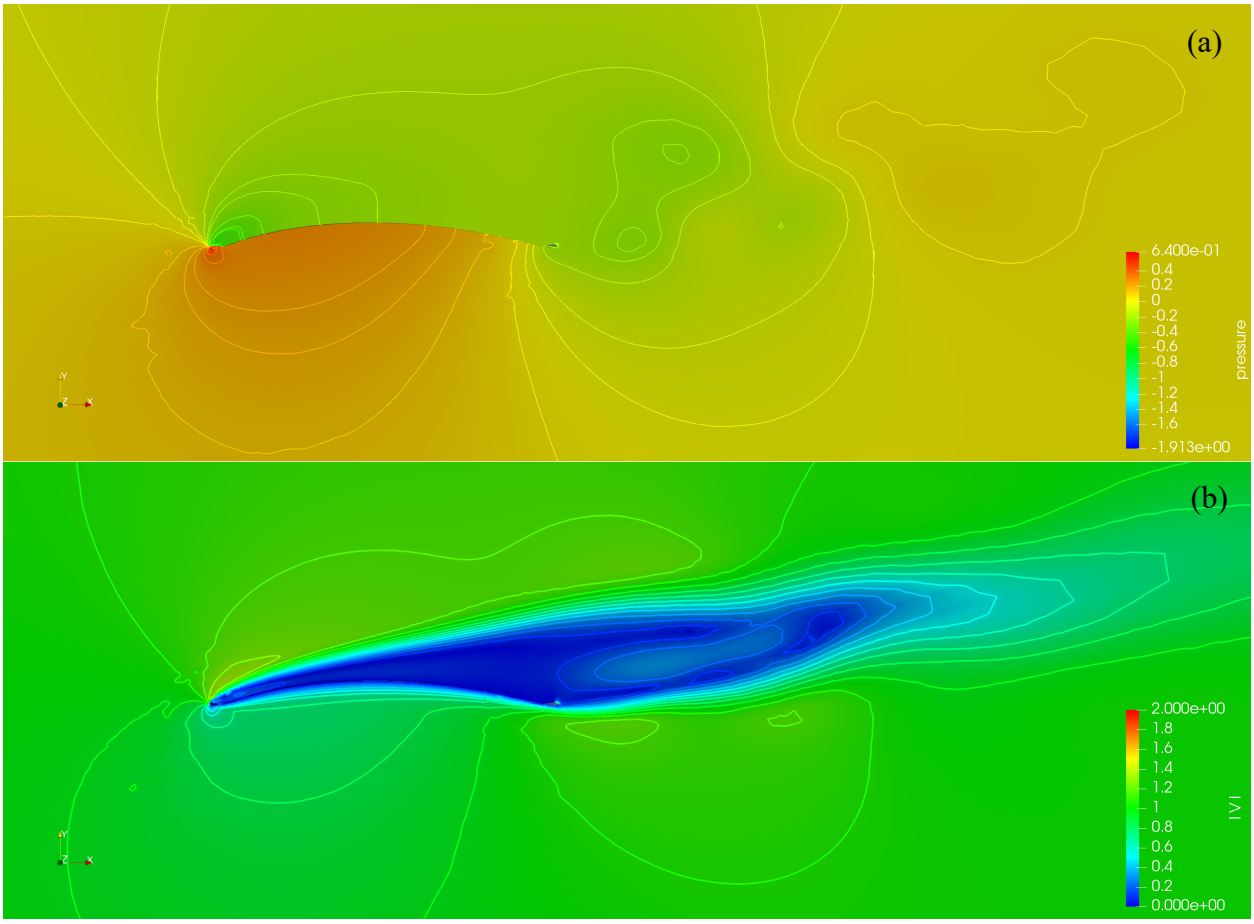

Fig. 8. Instantaneous (a) pressure and (b) magnitude of velocity contours for the flow past the membrane at a = 12°. Re = 2500, using the implicit scheme.

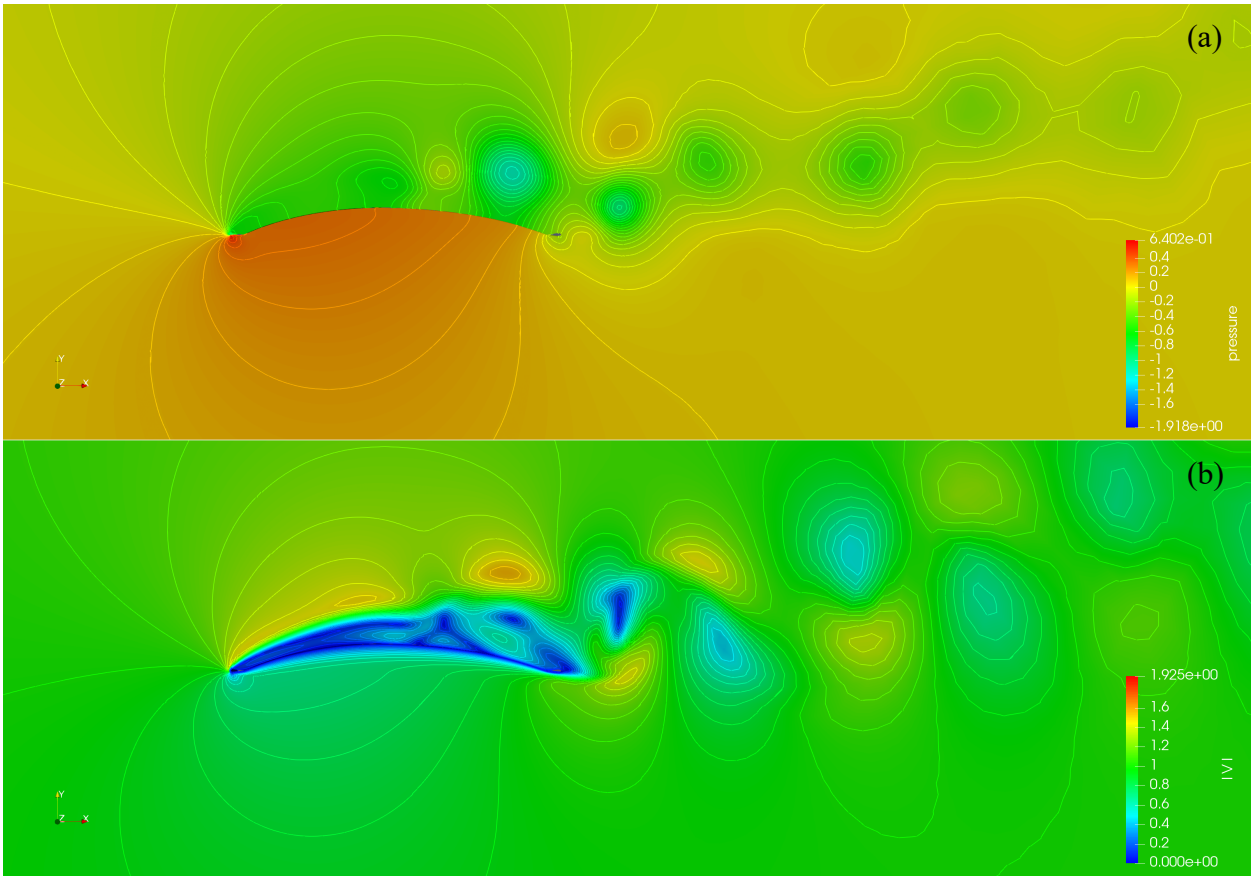

Fig. 9. Instantaneous (a) pressure and (b) magnitude of velocity contours for the flow past the memebrane at $\alpha = 12°$. Re = 2500, using the explicit scheme.

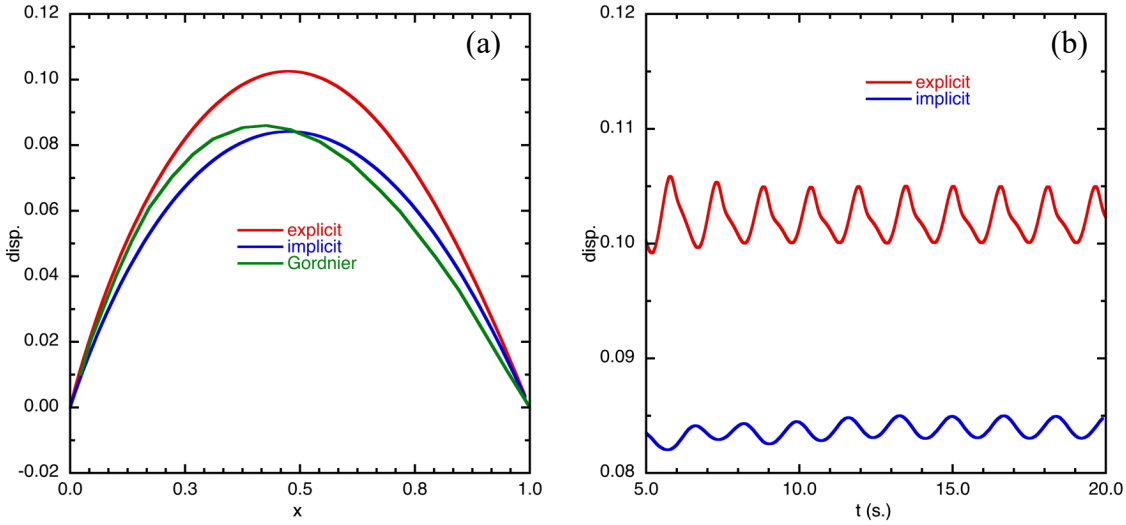

Fig. 10. Results for the membrane deflection for $\alpha = 16°$, (a) comparison of the mid-chord displacement, and (b) comparison of the mean deflection.

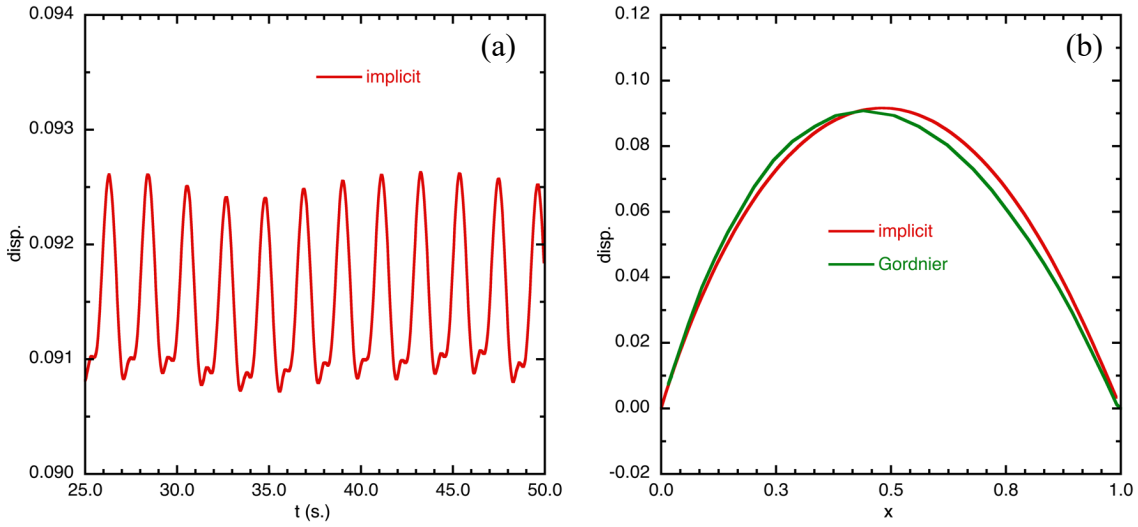

Fig. 11. Results for the membrane deflection for $\alpha = 20°$, (a) time history of the mid-chord displacement, and (b) comparison of the mean deflection.

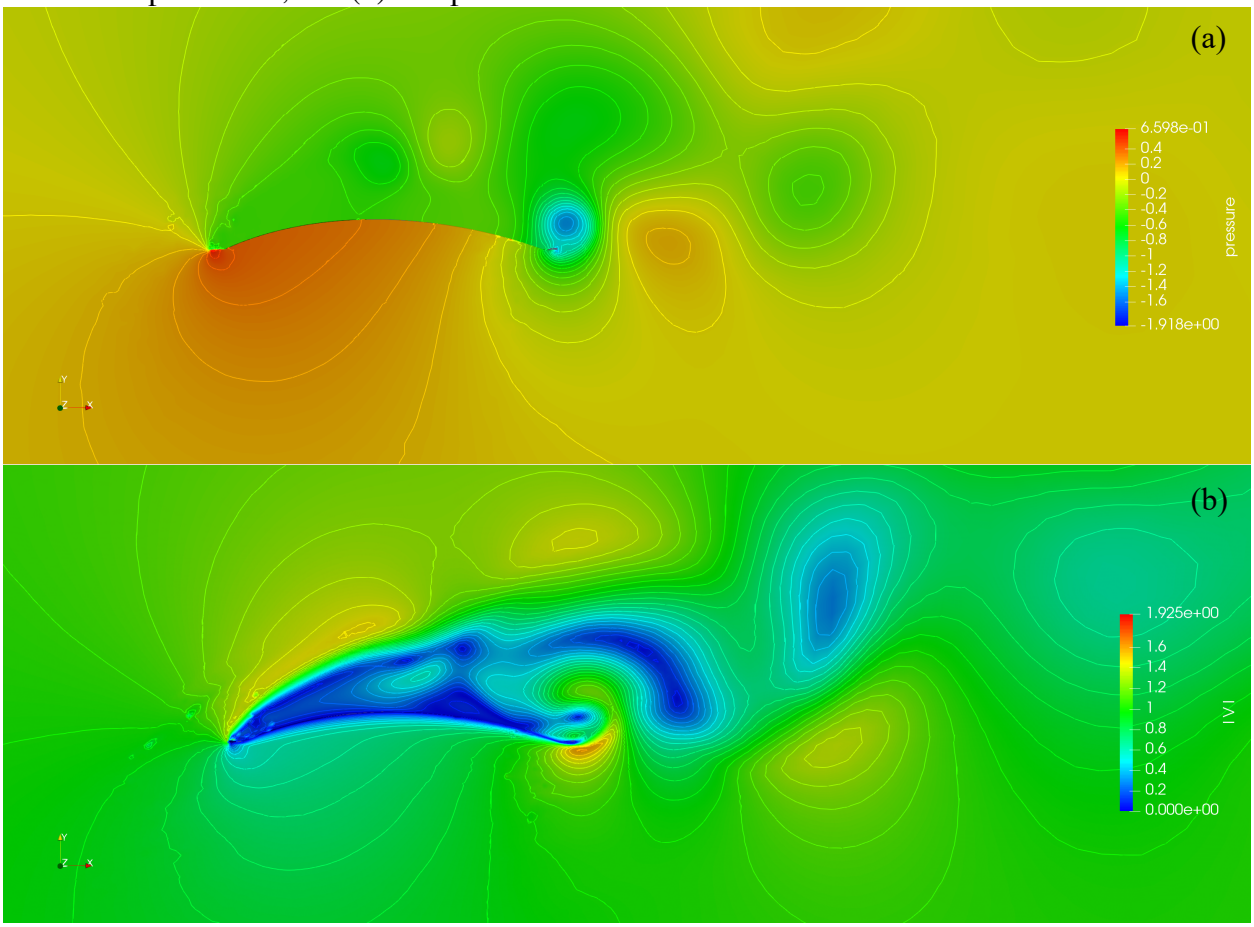

Fig. 12. Instantaneous (a) pressure and (b) magnitude of velocity contours for the flow past the memebrane at $\alpha = 20°$. Re = 2500, using the implicit scheme.

oscillation, but the implicit scheme does, as shown in Fig. 11a. Again, the comparison with the results for this case is good. Figure 12 shows the instantaneous pressure and velocity contours at the end of the simulation.

Coupling with a Comprehensive CSD Code:

Most natural flyers such as bats use an articulated skeleton covered with elastic membrane for morphing their wings during flight. In this research effort, we consider bio-inspired wings comprised of carbon fiber structures and elastic Mylar membrane between them. A coupled CFD-Computational Structural Dynamics (CSD) solver was developed for this purpose. The structural solver, ASICSD, is a finite element code intended to model large structural deformations. The spatial discretization is performed via unstructured grids of finite elements that can be of 0-D (point masses), 1-D (beams, trusses), 2-D (shells, plates) or 3-D (solid) topology. The temporal integration is explicit. The code incorporates a large library of materials and various equations of state (EOS), as well as many kinematic options, such as slide lines and contacts. After each time step, ASICSD obtains all the 'wetted faces' and makes them available to the flow solvers.

The Lagrangian dynamic equilibrium equation written on the spatial configuration at time *t* (Ω_t) is given by

$$\rho\ddot{\mathbf{u}} - \nabla \cdot \sigma = \mathbf{f} \quad \text{in } \Omega_t, \tag{26}$$

with the compatible initial and boundary conditions. The Cauchy stress tensor σ is obtained from a constitutive material equation. In Eq. (26), ρ is the density of the material, **u** the displacement field, $\ddot{\mathbf{u}}$ the acceleration and **f** the body force.

The equilibrium variational form at the spatial configuration is obtained by multiplying Eq. (26) by a test function $\delta\mathbf{u} \in \mathrm{V}$ that fulfills the imposed boundary condition and continuity requirements. After integrating by parts, the following is obtained

$$\int_\Omega \rho\delta\mathbf{u} \cdot \ddot{\boldsymbol{u}} = -\int_\Omega \epsilon(\delta\mathbf{u}) : \sigma d\Omega + \int_\Omega \delta\mathbf{u} \cdot \sigma d\Omega + \int_{\Gamma_N} \delta\mathbf{u} \cdot \mathbf{t} d\Gamma, \quad \forall\, \delta\mathbf{u} \in \mathrm{V}, \tag{27}$$

where $\epsilon(\cdot)$ is the spatial symmetric gradient operator. $\epsilon(\delta\mathbf{u})$ is the spatial strain rate tensor, which is obtained from the standard finite element kinematic interpolation, **t** is the surface traction tensor applied on the boundary of Ω ($\partial\Omega$)in the actual configuration, and Γ_N is the normal Neumann part of $\partial\Omega$. Following the finite element approximation, Eq. (27) can be written as

$$\mathbf{M}\ddot{\mathbf{u}} + \mathbf{D}\dot{\mathbf{u}} + \mathbf{K}\mathbf{u} = \mathbf{f} \quad , \tag{28}$$

where **M** is the standard mass matrix, **D** the damping matrix, **K** the stiffness matrix, and f the external force. Eq. (28) is discretized in time with the standard Newmark method. Given the solution at t^{n-1}, the solution at t^n can be obtained from

$$\mathbf{u^n} = \mathbf{u^{n-1}} + \Delta t\dot{\mathbf{u}}^{n-1} + \frac{\Delta t^2}{2}[(1-2\beta)\ddot{\mathbf{u}}^{n-1} + 2\beta\ddot{\mathbf{u}}^n], \tag{29}$$

$$\dot{\mathbf{u}}^{\mathbf{n}} = \dot{\mathbf{u}}^{\mathbf{n-1}} + \Delta t[(1-\gamma)\ddot{\mathbf{u}}^{n-1} + \gamma\ddot{\mathbf{u}}^n] \quad , \tag{30}$$

where Δt is the time step and β and γ are scalar parameters. With $\beta = 0$, we get an explicit scheme, the stability of which is dependent on the Δt.

Application to Notional Flapping Wing Vehicle:

The flapping wing prototype we chose to test this coupled solver was developed by researchers at Stanford University [14]. The wing consists of a hinged leading edge and flexible spars, all made of carbon fiber, over which a thin Mylar membrane is stretched and which allows for decoupled membrane deformation betweeen them, as shown in Fig. 13. The carbon fiber rods are of various diameters as shown in Fig. 13, with a Young's modulus E =140GPa and a Poisson's ratio $\nu = 0.45$. The mylar film is 0.05cm thick with E= 4GPa and $\nu = 0.35$. The carbon fiber beams were discretized using Hughes-Liu beam elements, while the mylar membrane is discretized using the MITC3 triangular elements.

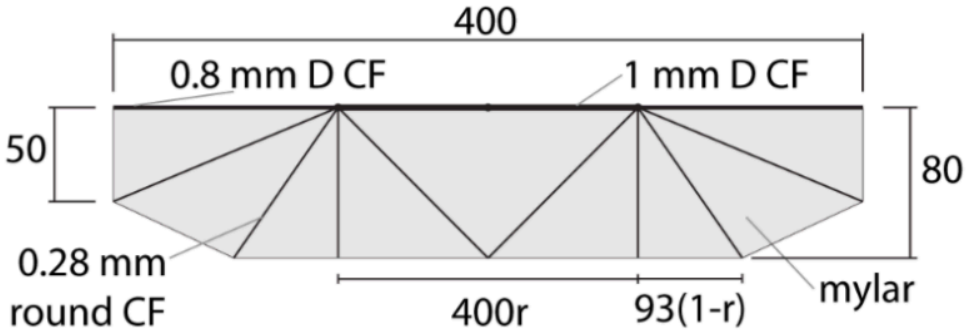

Fig. 13. Fully extended wing planform of the Stanford DelFly robot.

In order to simulate a realistic vehicle with flapping wings, a cylindrical body was added. Simulations over this configuration, shown in Fig. 14, are performed with the vehicle moving at a velocity of 1 Chord/sec. Several parametric studies varying the amplitude, frequency of the flapping wing, in addition to the location of actuation of the wing either at the leading edge of the root or the entire chord along the root are performed. This configuration was used earlier for the development of a coupled CFD-Control tool [15], in which the kinematics of the flapping wings were prescribed from experimental studies. In this work, the motion of the leading edge tip and the elbow joint are monitored. Some of the results are discussed next.

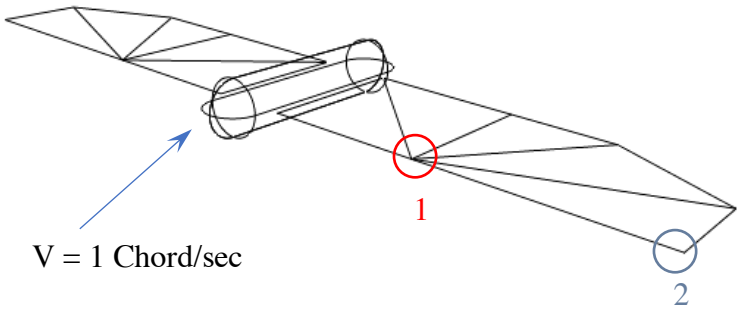

Fig. 14. Notional flapping wing vehicle configuration.

First, the wing was actuated at one point, the root of leading edge spar, with an amplitude of $\Phi = \pm 30°$ and a sinusoidal flapping frequency of 12.5Hz. In comparison, the experimental studies, were performed with the stroke amplitude of the wing was nearly 25° and a flapping frequency of 14Hz. Figure 15 shows the force time history of thrust production and the excursion of the two

leading edge points. From Fig. 15a, the mean thrust at the vehicle speed of 8cm/s is nearly zero, implying that the vehicle will be able to fly at this speed given this kinematics for flapping. Figure 15b shows that the elbow and the tip of the leading edge are nearly 180° out of phase. Fig. 16 shows the pressure distribution on the surface of the wing at an instant t = 1.939s, when the two leading edge points are moving in opposite directions. Varying the outer leading edge spar thickness and the Young's modulus did not significantly change the phasing between the leading edge points. The flapping frequency was reduced to 5Hz and the results showed that the mean thrust increased to nearly 0.03N and the displacement of the points along the leading edge are more than doubled as compared to 12.5Hz and, furthermore are in phase, as shown in Fig. 17.

Next, the wing was actuated along the entire root chord. For a pitch amplitude of 30°, the flapping wings achieve a maximum mean thrust of 0.03N at 5Hz, and the mean thrust decreases with increase in flapping frequency to 12.5Hz, as shown in Fig. 18a. Figure 18b shows the displacement of the leading edge tip (solid line) and the elbow joint (dotted line) for the three frequencies tested. The leading edge tip displacement is nearly doubled as the frequency is increased from 2.5Hz to 5.0Hz and reduces as the frequency is further increased. At the lower frequencies, both the leading edge points are in phase and nearly 180° out of phase at f = 12.5Hz.

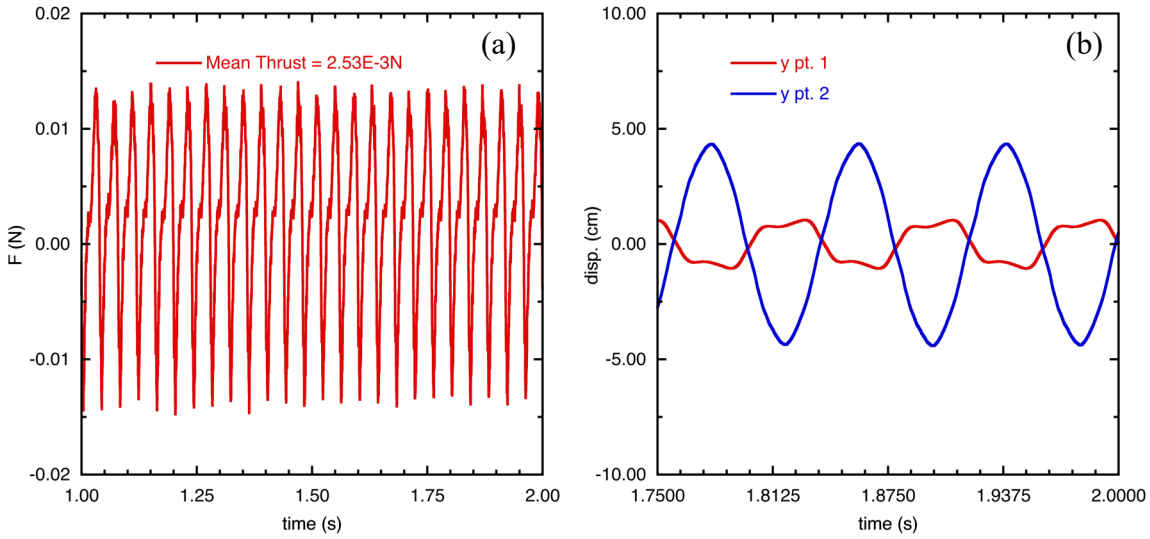

Fig. 15. Time histories for the notional flapping wing vehicle at f = 12.5Hz, Φ = ±30°, (a) thrust and (b) displacement of the leading edge elbow and tip.

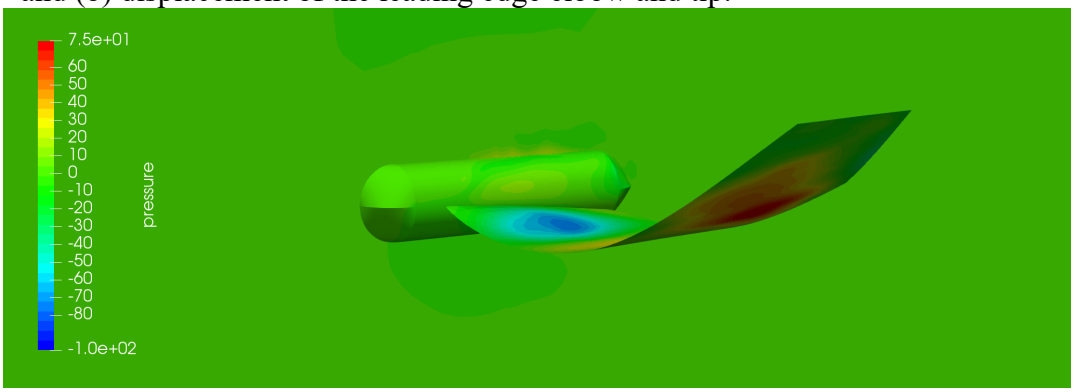

Fig. 16. Surface pressure distribution on the flapping wing at t= 1.939s.

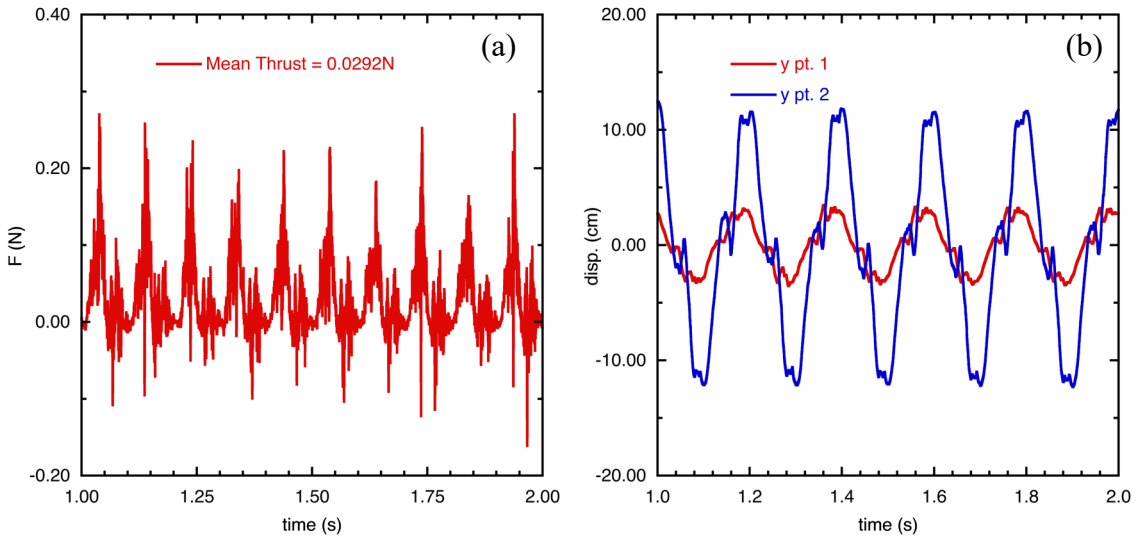

Fig. 17. Time histories for the notional flapping wing vehicle at f = 5Hz, Φ = ±30°, (a) thrust and (b) displacement of the leading edge elbow and tip.

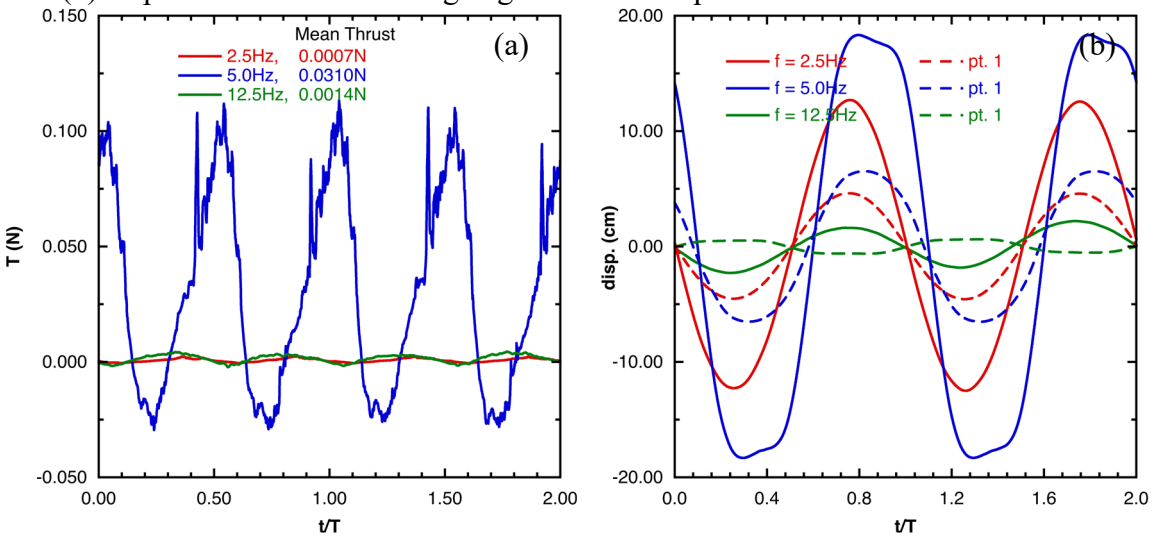

Fig. 18. Time histories of (a) thrust and (b) displacement of the leading edge points for the flapping wing, Φ = ±30°.

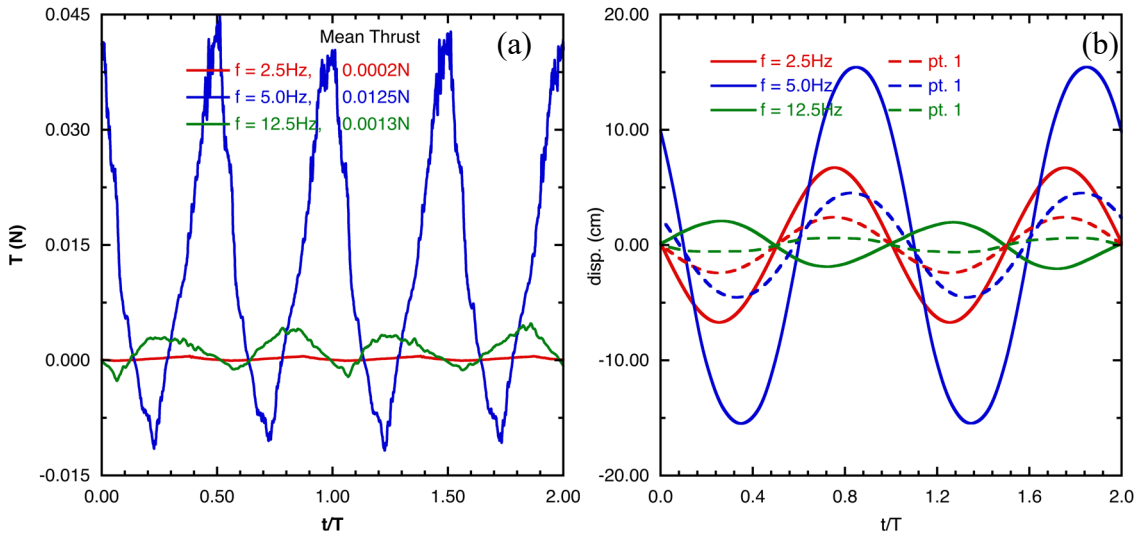

Fig. 19. Time histories of (a) thrust and (b) displacement of the leading edge points for the flapping wing, $\Phi = \pm 15°$.

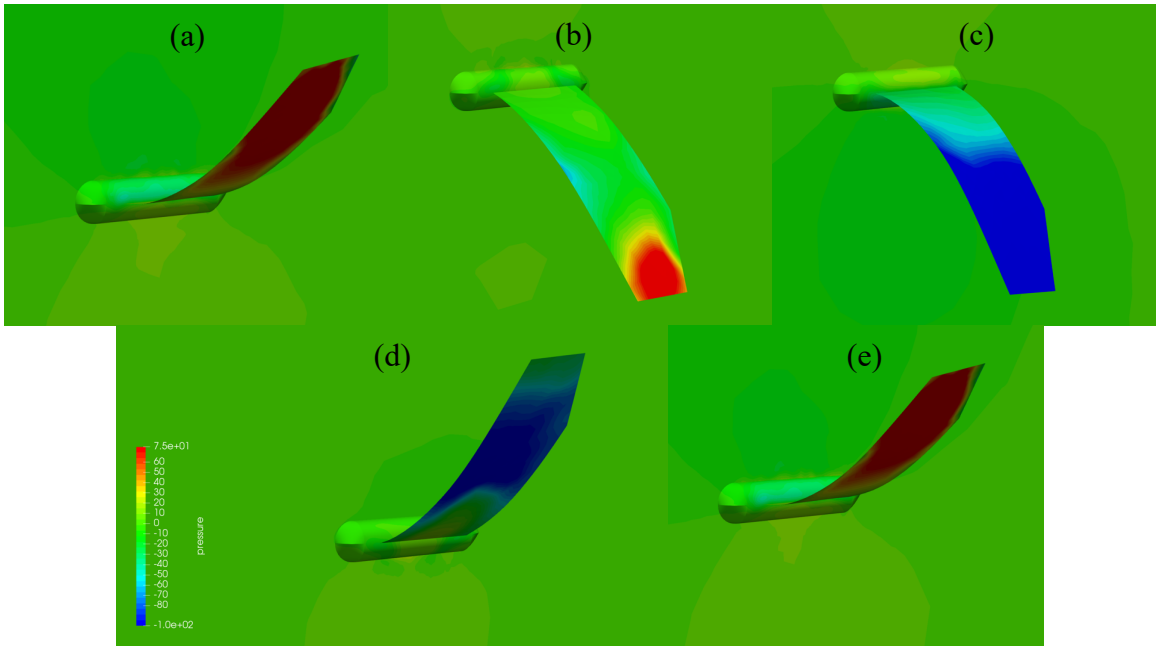

Fig. 20. Surface pressure distribution on the flapping wing at the extrema of thrust production during one flapping cycle, $\Phi = \pm 15°$, f = 5.0Hz, (a) t/T= 0.0, (b) 0.215, (c) 0.48, (d) 0.73 and (e) 1.0.

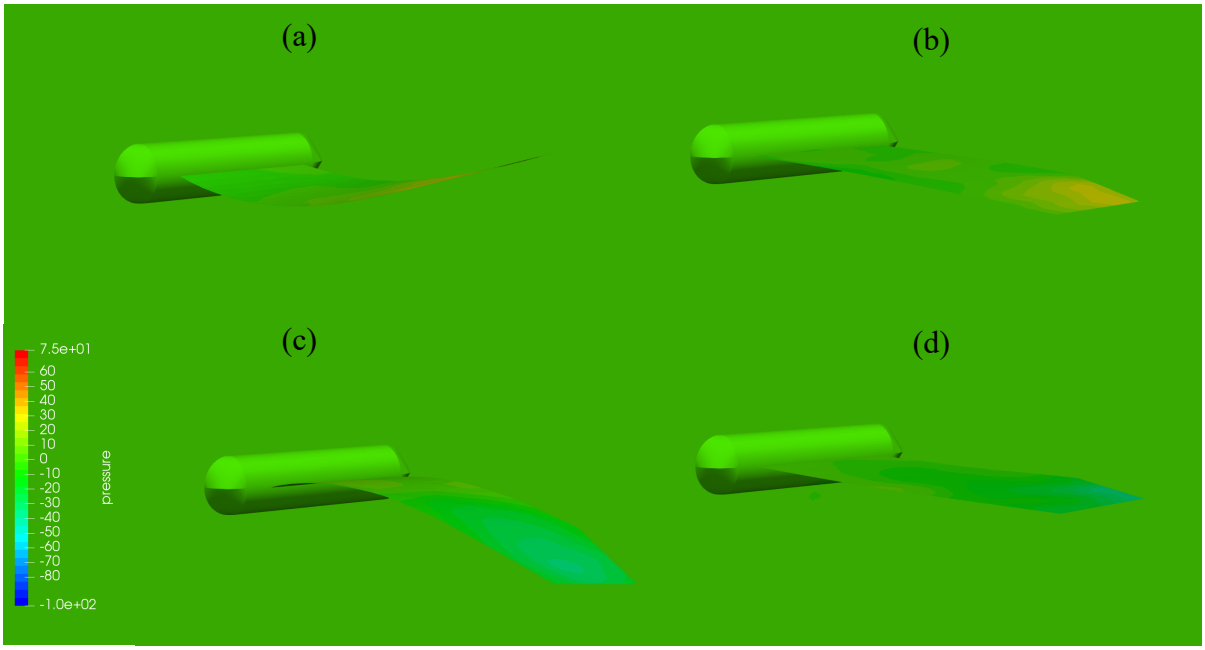

Fig. 21. Surface pressure distribution on the flapping wing at the extrema of thrust production during one flapping cycle, $\Phi = \pm 15°$, f = 12.5Hz, (a) t/T= 0.25, (b) 0.5, (c) 0.75, and (d) 1.0.

A similar trend is observed for a stroke amplitude of 15°, with the maximum mean thrust at f = 5.0Hz being reduced to 0.0125N, shown in Fig. 19. Figures 20 and 21 show the wing deformation and the surface pressure distribution corresponding to the minimum and maximum thrust production instants shown in Fig. 19 at the flapping frequency of 5Hz and 12.5Hz, respectively. At 12.5Hz, the leading edge spars appear to be dominated by the second mode of oscillation of a cantilevered beam and hence, the two points are out of phase. This needs to be verified by computing the eigenmodes of the entire wing and using the first coupled solver described here. Also, in the experimental studies of this flapping wing vehicle, the wing folds along the elbow during the stroke. In order to simulate this, additional joint boundary conditions need to be implemented, which is outside of the scope of this effort.

SUMMARY AND FUTURE WORK

A CFD solver was coupled to three different structural solvers in order to simulate flexible flapping wing dynamics. The first one was based on eigen modes and was validated using the Turek-Hron problem of elastic beam structures behind a cylinder at various Re. The comparison was good for both Re = 20 and the unsteady case of Re = 200. The second solver used a membrane model for the structure and was validated against results in the literature for various angles of attack. The third, a comprehensive nonlinear finite element structural solver was coupled to the CFD solver and tested for the simulation of flapping wings with both carbon fiber beams and mylar membranes. Several parametric studies varying the amplitude and frequency of the flapping wing were performed, and the maximum thrust production was found to be at 5Hz for a vehicle moving at a velocity of 1 chord/s. For this flapping wing vehicle, additional joint boundary conditions and the capability to allow for collapsible membranes, need to be incorporated in order to compare with the experimental studies. Another approach will be to simulate this complex fluid structure interaction using the eigen modes for this configuration and use the coupled solver described in this report.

ACKNOWLEDGEMENTS

This work was supported by NRL 6.1 base program on "Computational Advances for Flexible Flapping Analysis." This work was supported in part by a grant of HPC time from the DoD HPC center for the NRL Intel Xeon clusters.

REFERENCES

1. Ramamurti, R. and Sandberg, W.C., "A Three-Dimensional Computational Study of the Aerodynamic Mechanisms of Insect Flight," *J. Exp. Biol.,* 205, 10, pp. 1507-1518, 2002.
2. Ramamurti, R. and Sandberg, W.C., "A computational investigation of the 3-D unsteady aerodynamics of *Drosophila* hovering and maneuvering," *J. Exp. Biol.*, 210, 5, pp. 881-896, 2007.
3. Viswanath, K., Nagendra, K., Cotter, J., Fauenthal, M., and Tafti, D.K. (2014), "Straight-line climbing flight aerodynamics of a fruit bat," *Phy. of Fluids*, 26, 021901.
4. R. Ramamurti, W.C. Sandberg, P. Vaiana, J. Kellogg and D. Cylinder, "Computational fluid dynamics study of unconventional air vehicle configurations," *The Aeronautical Journal,* Vol. 109, No. 1097, pp. 337-347, July 2005.
5. Ramamurti, R., Geder J.D., Sandberg W.C., and Flynn, A., "Computational Fluid Dynamics Studies of a Flapping Wing Nano Air Vehicle," AIAA-2010-8117, AIAA Atmospheric Flight Mechanics Conference, Toronto, ON, Canada, August 2010.
6. Ramamurti, R. and Löhner, R., "Evaluation of an Incompressible Flow Solver Based on Simple Elements," *Advances in Finite Element Analysis in Fluid Dynamics*, FED 137, Editors: Dhaubhadel, M. N. *et al*., ASME Publication, New York,1992, pp. 33-42.
7. Ramamurti, R., Löhner, R., and Sandberg, W. C., "Computation of the 3-D Unsteady Flow Past Deforming Geometries," *Int. J. Comp. Fluid Dyn.*, 13, 1999, pp. 83-99.
8. S. Turek and J. Hron, "Proposal for Numerical Benchmarking of Fluid-Structure Interaction between an Elastic Object and a Laminar Incompressible Flow," *Fluid-Structure Interaction*, Springer Lecture Notes in Computational Science and Engineering, Vol. 53, Ed. H.-J. Bungartz & M. Schaefer, Springer Verlag 2006.
9. Numerical Benchmarking of Fluid-Structure Interaction: A comparison of different discretization and solution approaches, Lecture Notes in Computational Science and Engineering, January 2010.
10. Computation of Unsteady Laminar Flow over a Flexible Two-Dimensional Membrane Wing, Smith, R. and Shyy, W., Physics of Fluids, Vol. 7, No. 9, 1995, pp. 2175–2184.
11. A method of computation for structural dynamics, Newmark, N.M., *Journal of the Engineering Mechanics Division*, 85 (EM3), 1959, pp. 67–94.
12. Rojratsirikul, P., Wang, Z., and Gursul, I., "Unsteady Aerodynamics of Membrane Airfoils," AIAA-2008-0613, 46th AIAA Aerospace Sciences Meeting, Reno, NV, January 2008.
13. Gordnier, R. E., "High Fidelity Computational Simulation of a Membrane Wing Airfoil," AIAA-2008-0614, 46th AIAA Aerospace Sciences Meeting, Reno, NV, January 2008.
14. A. Stowers and D. Lentink, Folding in and out: passive morphing in flapping wings, *Bioinspiration & Biomimetics*, 10 205001, March 2015.
15. Geder J.D., Ramamurti R., and Viswanath, K., "Simulation of a Flapping Wing UAV using a Coupled CFD-Control Tool," AIAA-2015-3151, AIAA Applied Aerodynamics Conference, Dallas, TX, 2015.